Supporting Information

Strain-mediated grain-boundary reconstruction unlocks high near-room-temperature thermoelectric performance in Mg_3Sb_2-based alloy

Gang Wu[1,3], Airan Li[1,3], Harish Subramania[1], Xinzhi Wu[1], Longquan Wang[1], Jiankang Li[1,2], Fei Frank Yun [1], Takao Mori[1,2*]

1. Research Center for Materials Nanoarchitectonics (MANA), National Institute for Materials Science (NIMS), Tsukuba, 305-0044, Japan.

2. Graduate School of Pure and Applied Science, University of Tsukuba, 1-1-1 Tennodai, Tsukuba, Ibaraki 305-8671, Japan.

3. These authors contributed equally to this work.

Corresponding author, email: MORI.Takao@nims.go.jp

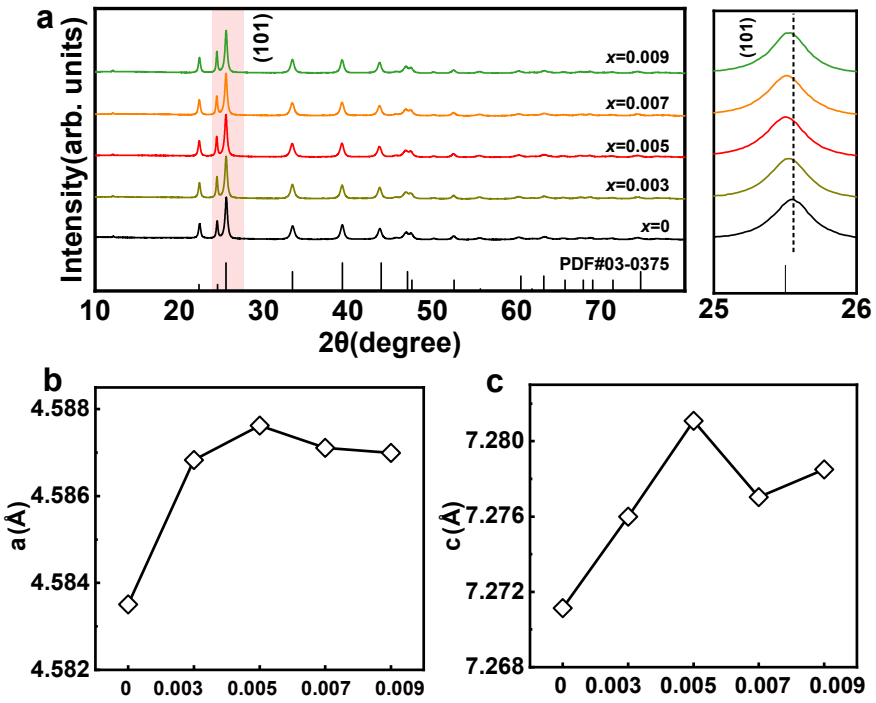

Supplementary Fig. 1. XRD patterns. a The XRD patterns of $Mg_{3.2(1-x)}Cu_xGa_xSb_{1.5(1-x)}Bi_{0.5(1-x)}Te_{2x}$ (x=0, 0.003, 0.005, 0.007, 0.009) samples at room temperature. The lattice parameters of **b** a-aixs and **c** c-aixs.

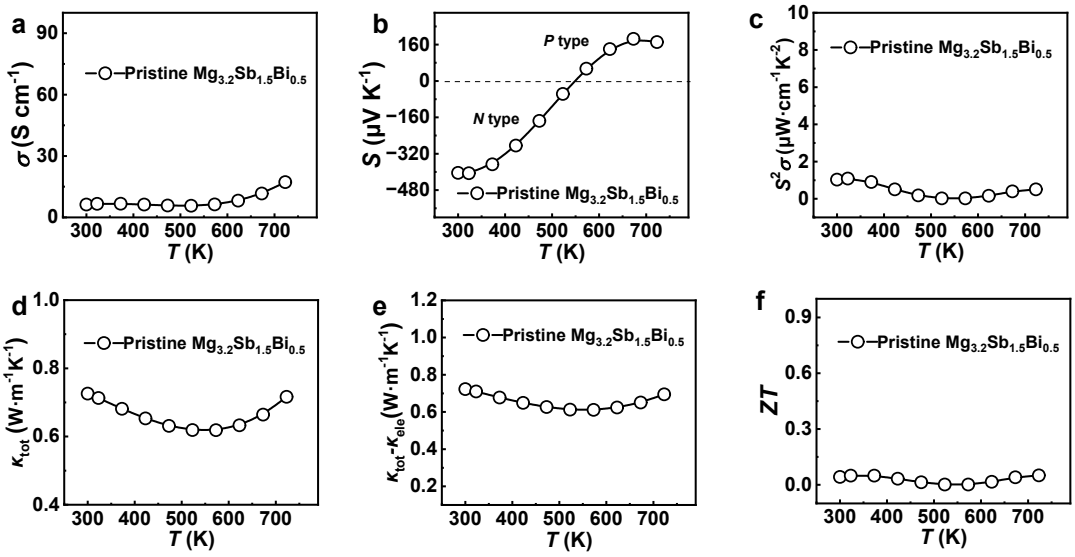

Supplementary Fig. 2. The thermoelectric properties of pristine sample. **a** σ, **b** S, **c** $S^2\sigma$, **d** κ_{tot}, **e** κ_{tot}-κ_{lat}, **f** ZT value.

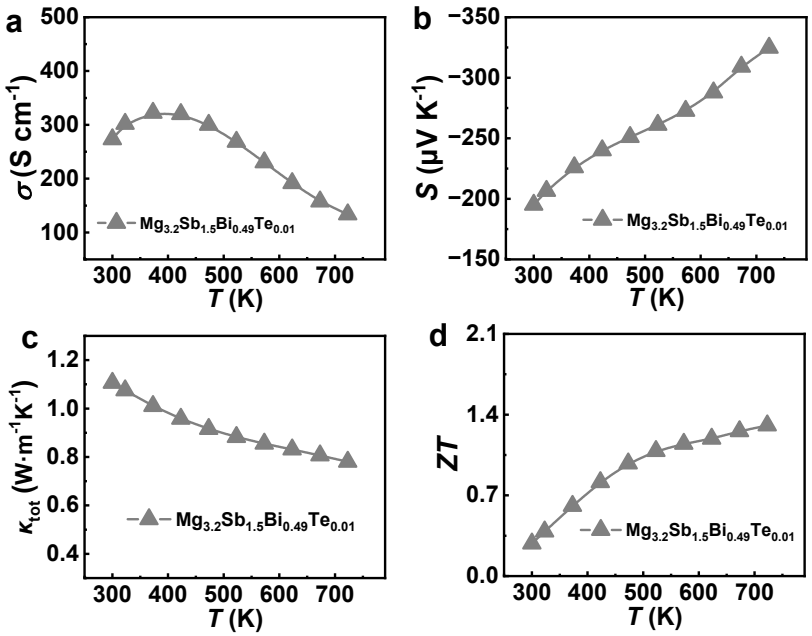

Supplementary Fig. 3. The thermoelectric properties of $Mg_{3.2}Sb_{1.5}Bi_{0.49}Te_{0.01}$. **a** σ, **b** S, **c** κ_{tot}, **d** ZT value.

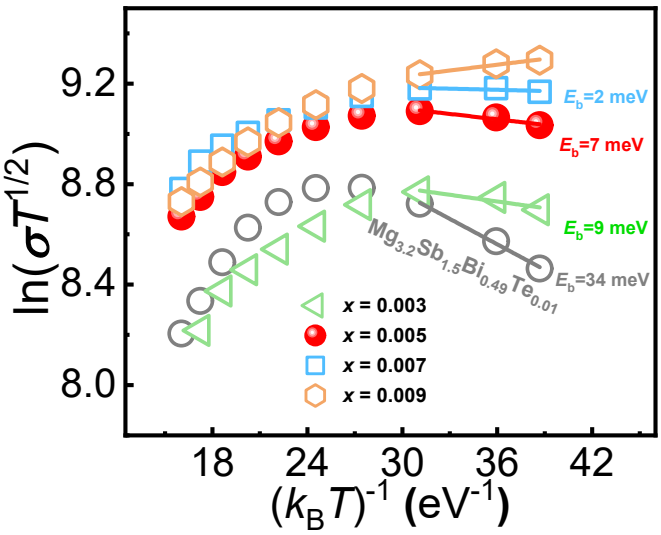

Supplementary Fig. 4. The calculated grain boundary potential barrier (E_b) by linear extrapolated from the $\ln(\sigma T^{1/2})$ as a function of $1/k_BT$ curve.

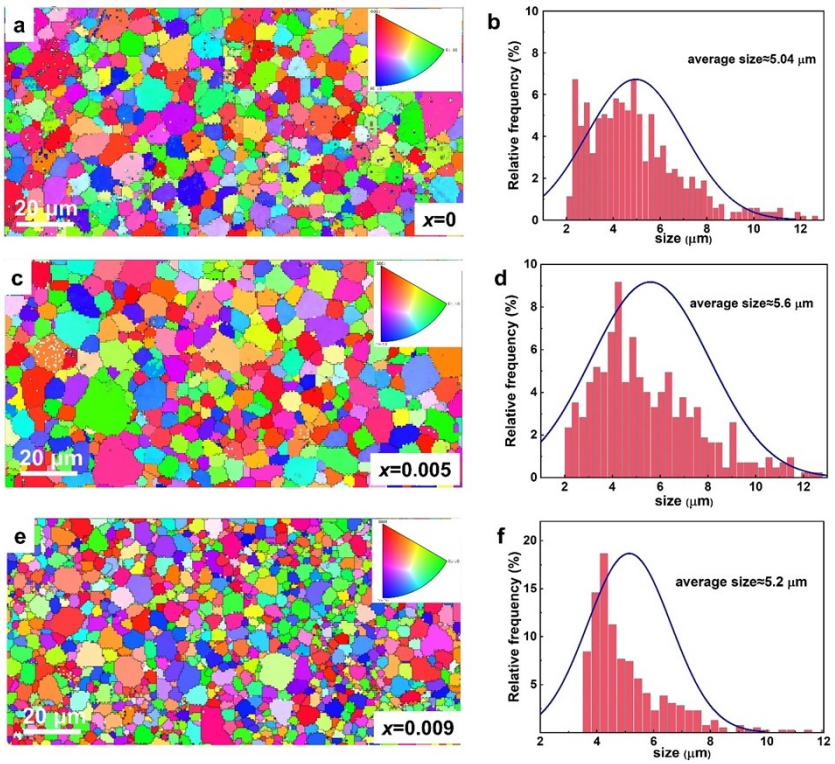

Supplementary Fig. 5. The microstructural evolution. The EBSD graphs and its grain size distribution, **a-b** x=0, **c-d** x=0.005, **e-f** x=0.009.

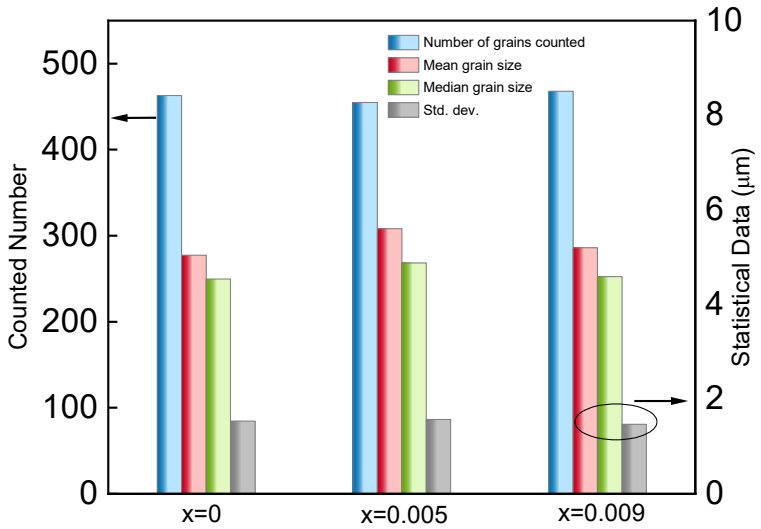

Supplementary Fig. 6. The number of grains counted, mean grain size, median grain size and standard deviation for x=0, x=0.005 and x=0.009 samples.

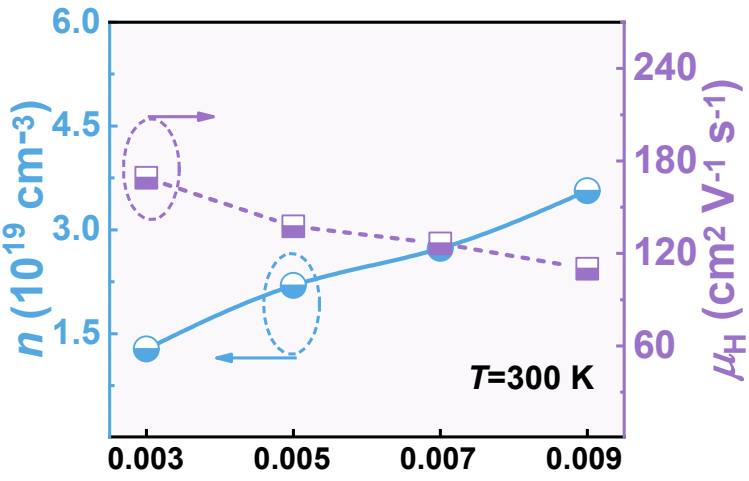

Supplementary Fig. 7. The changes in carrier concentration (n) and carrier mobility (μ) of samples.

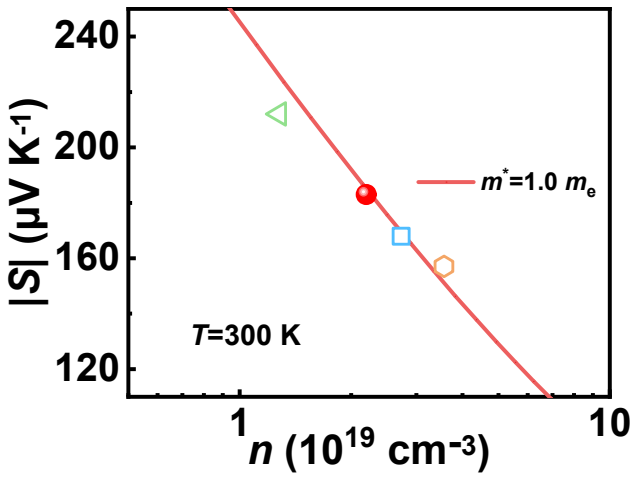

Supplementary Fig. 8. The curve between carrier concentration and Seebeck coefficient based on single parabolic band model.

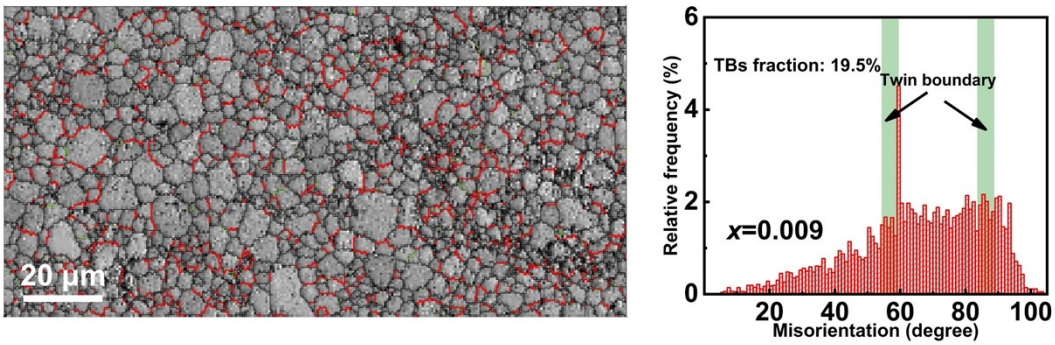

Supplementary Fig. 9. The grain misorientation distributions and corresponding morphology maps for x=0.009 sample. TBs are marked in red.

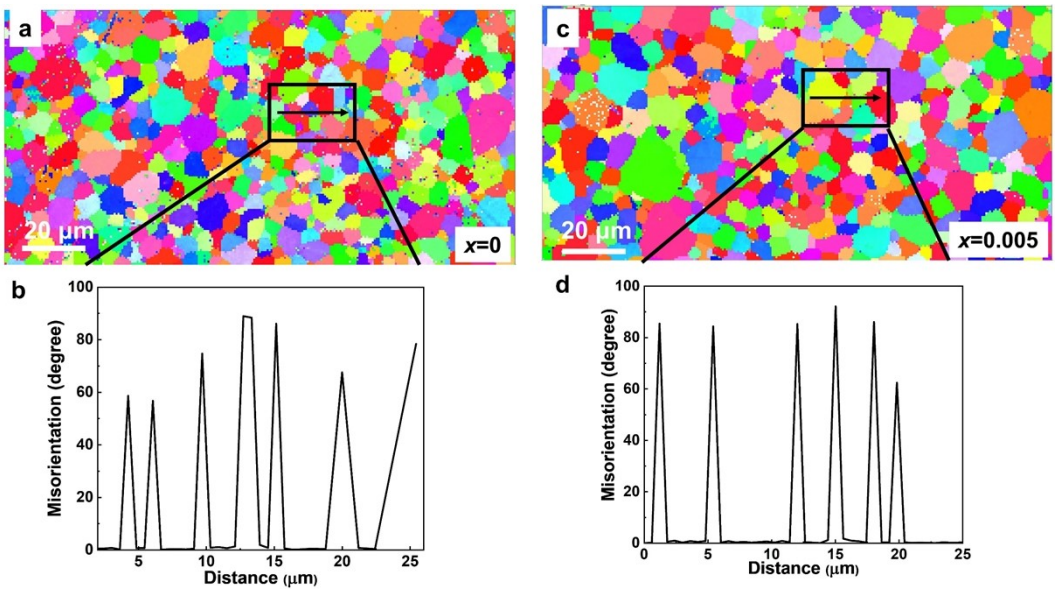

Supplementary Fig. 10. The magnified misorientation analysis for **a**-**b** x=0, and **c**-**d** x=0.005.

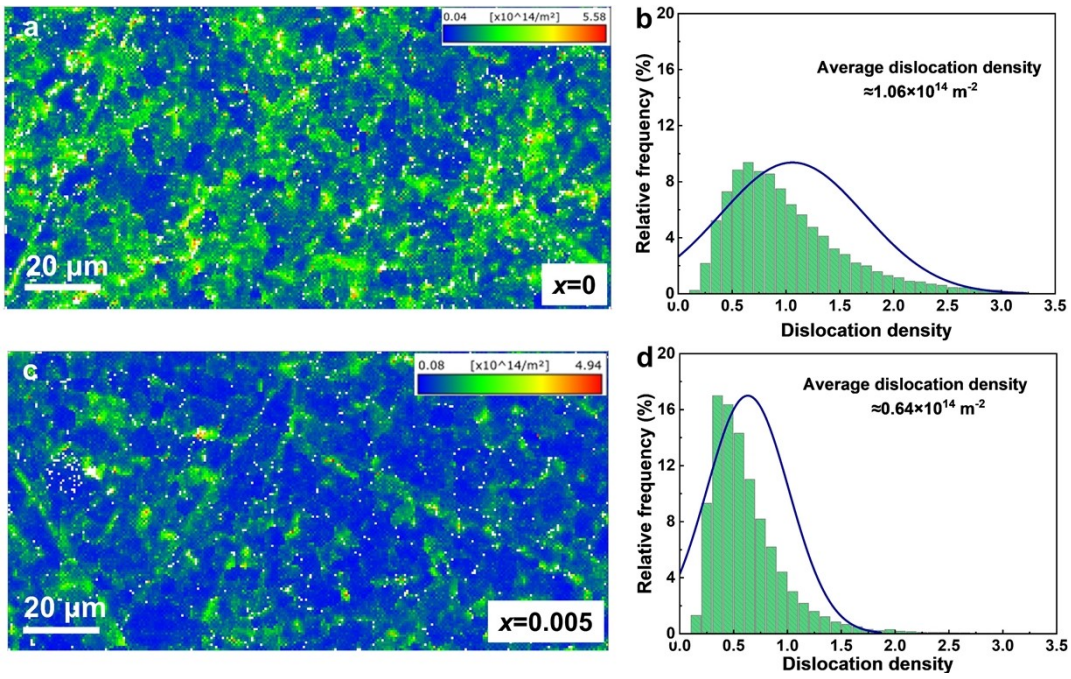

Supplementary Fig. 11. The dislocation density distribution for **a**-**b** x=0, and **c**-**d** x=0.005.

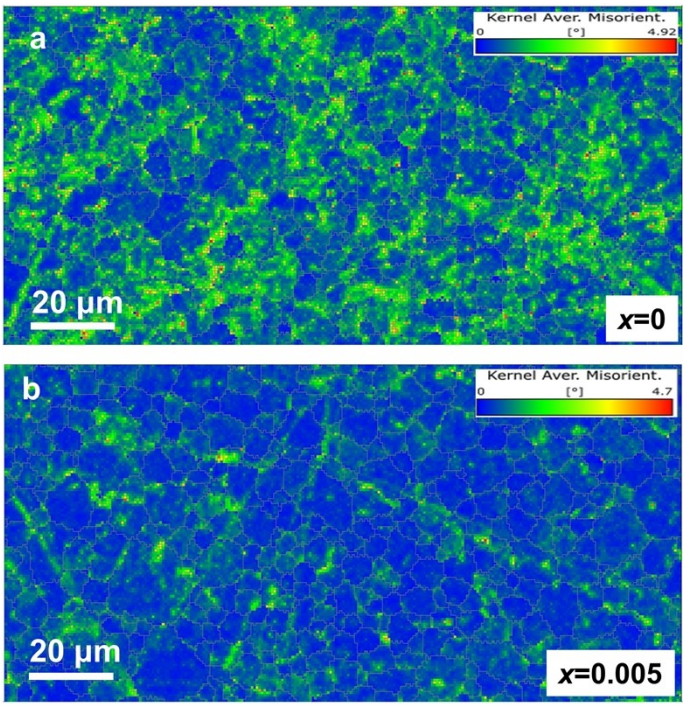

Supplementary Fig. 12. The Kernel Average Misorientation distribution map for **a** x=0 and **c** x=0.005 samples.

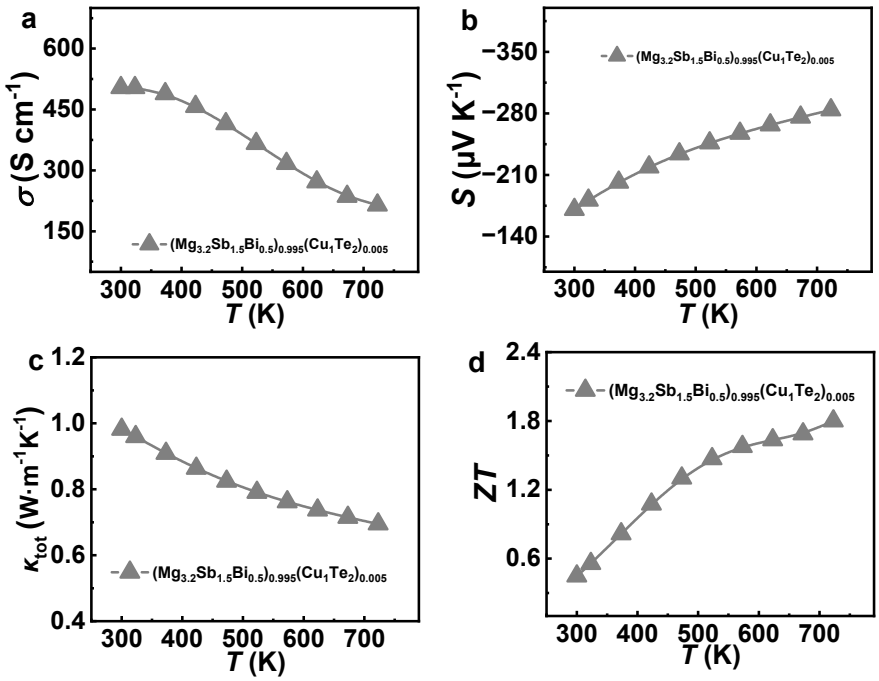

Supplementary Fig. 13. The thermoelectric properties of nominal component $(Mg_{3.2}Sb_{1.5}Bi_{0.5})_{0.995}(Cu_1Te_2)_{0.005}$ sample. **a** σ, **b** S, **c** κ_{tot}, **d** ZT value.

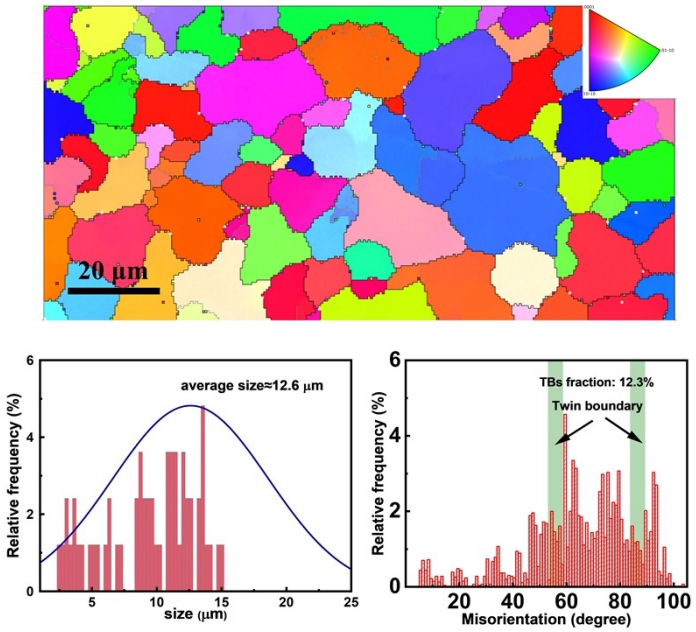

Supplementary Fig. 14. The grain size and grain misorientation distributions for nominal component $(Mg_{3.2}Sb_{1.5}Bi_{0.5})_{0.995}(Cu_1Te_2)_{0.005}$ sample.

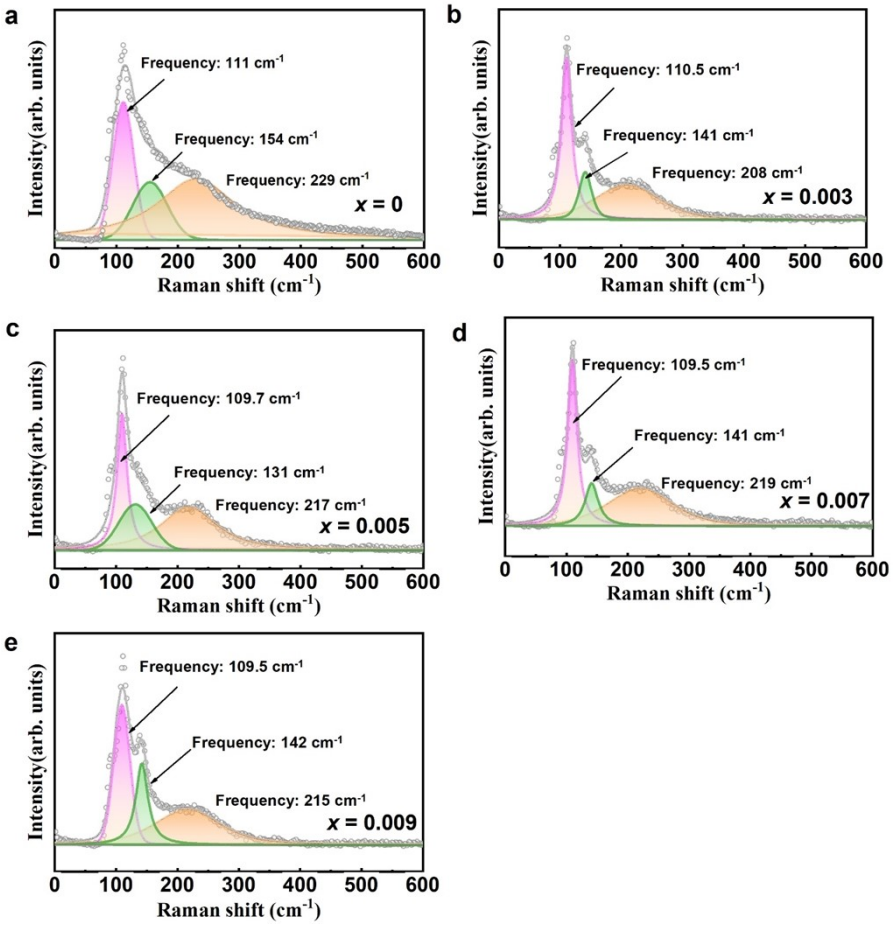

Supplementary Fig. 15. Raman spectrum for the x=0, 0.003, 0.005, 0.007, 0.009 samples at room temperature.

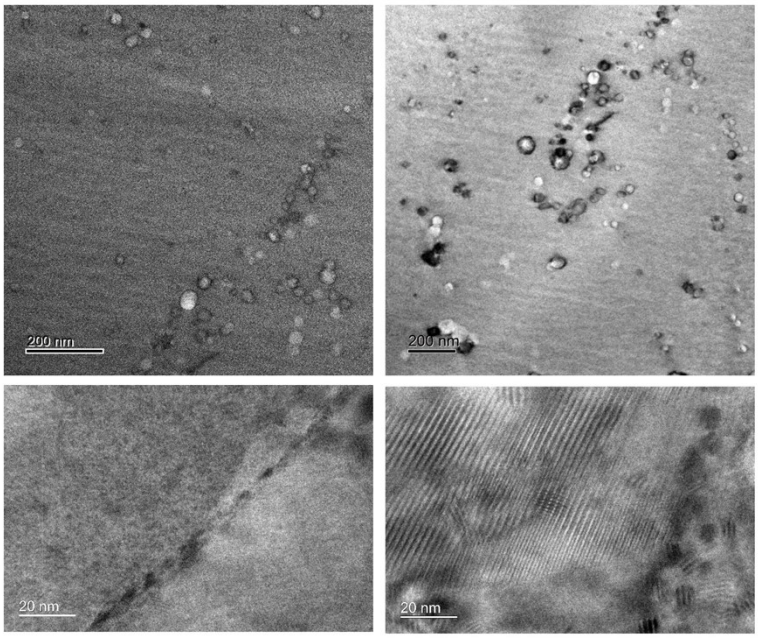

Supplementary Fig. 16. The STEM microstructural analysis of the x=0.005 sample.

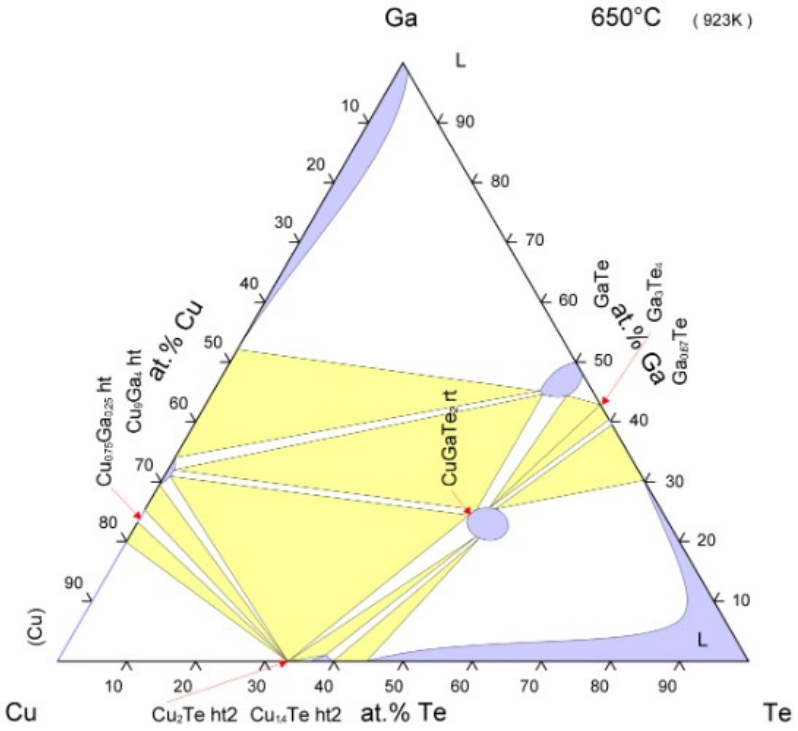

Supplementary Fig. 17. Isothermal Cu-Ga-Te ternary phase diagram at 923 K, illustrating the equilibrium phase fields and tie-triangle regions involving $CuGaTe_2$ and Cu-Ga-rich phases.[1]

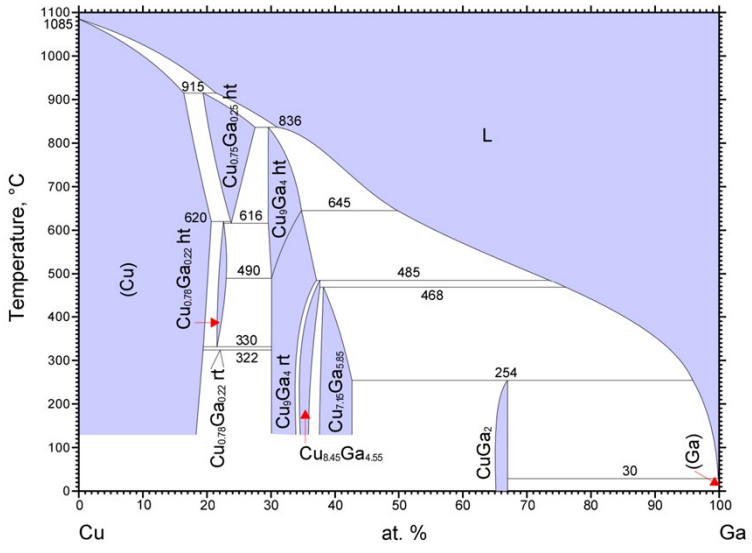

Supplementary Fig. 18. Binary Cu-Ga phase diagram showing the equilibrium phase regions and stable intermetallic compounds (Cu_9Ga_4, $Cu_{0.78}Ga_{0.22}$, $CuGa_2$), providing thermodynamic guidance for identifying Cu-Ga precipitates.[2]

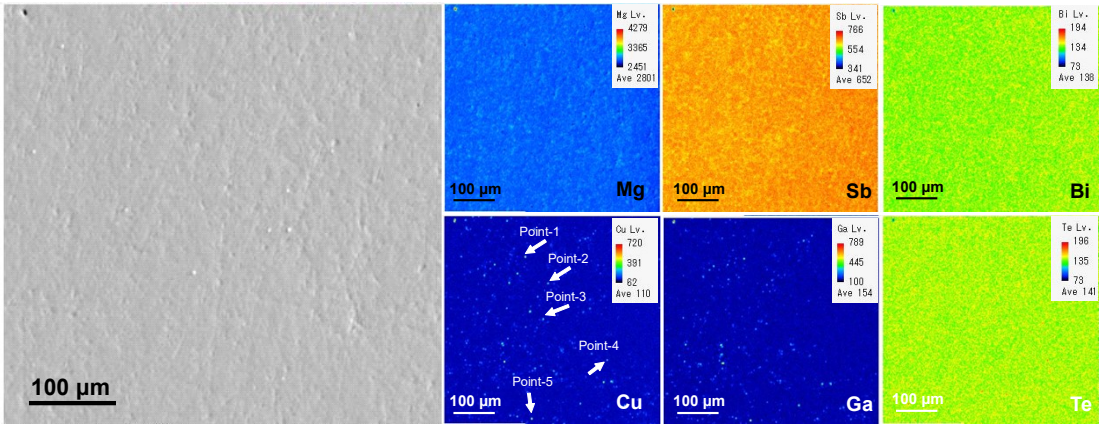

Supplementary Fig. 19. The EPMA elemental mapping of the x=0.005 sample showing homogeneous distributions of Mg, Sb, Bi and Te, while Cu and Ga exhibit localized enrichment, indicating the formation of ultrafine Cu-Ga precipitates.

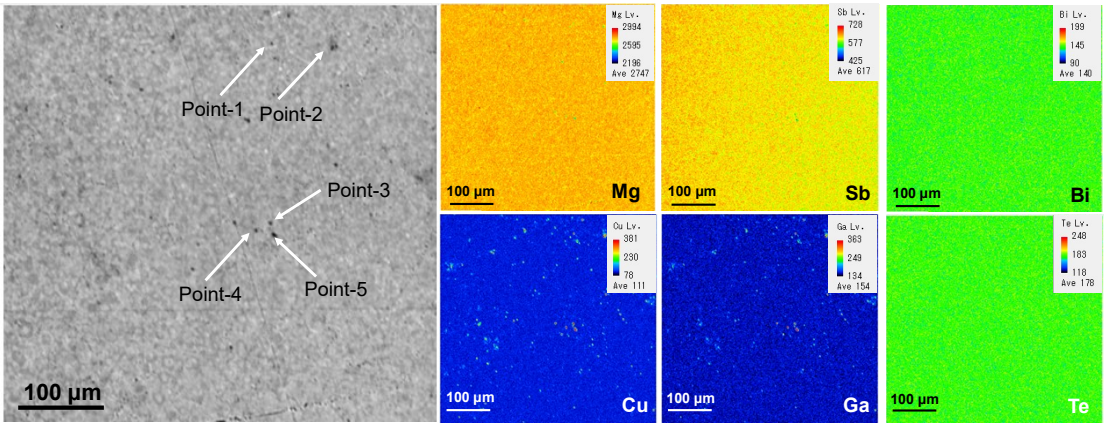

Supplementary Fig. 20. The EPMA elemental mapping of the x=0.009 sample showing homogeneous distributions of Mg, Sb, Bi and Te, whereas Cu and Ga exhibit pronounced large localized enrichment, indicating the formation of micron-sized Cu-Ga precipitates.

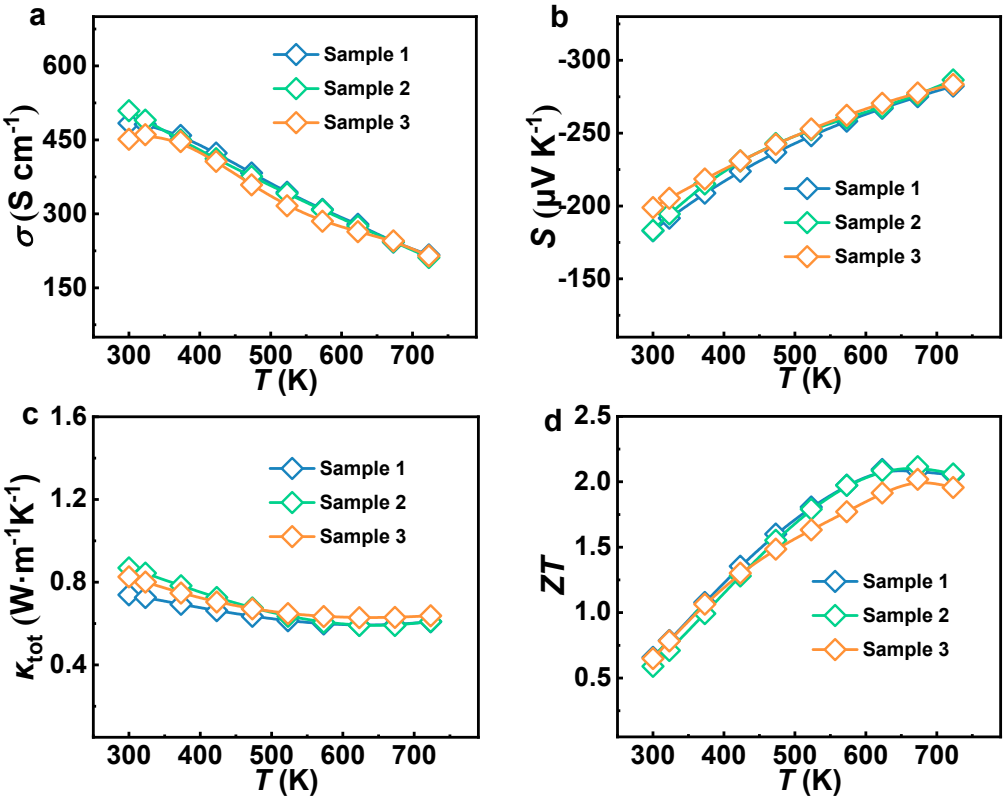

Supplementary Fig. 21. The thermoelectric properties of multiple samples with the same composition x=0.005. **a** σ, **b** S, **c** κ_{tot}, **d** ZT value.

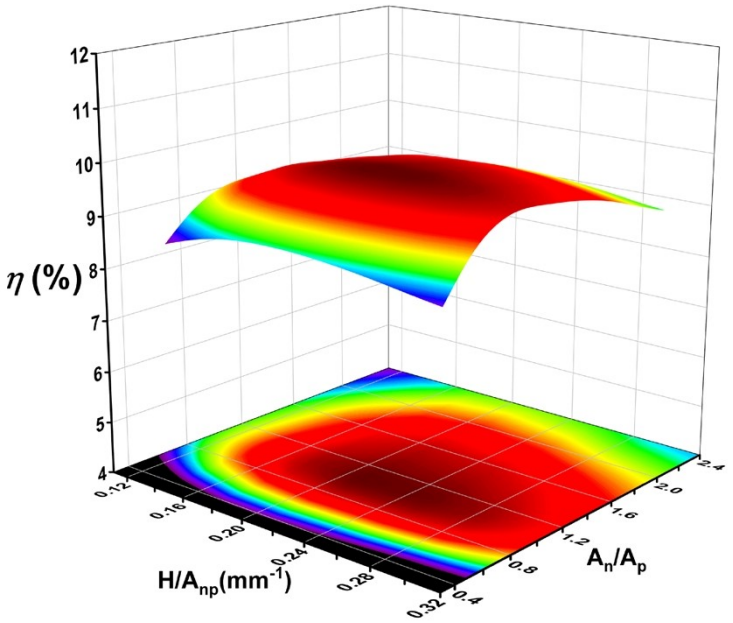

Supplementary Fig. 22. Theoretical conversion efficiency (η) as a function of module height and cross-sectional area.

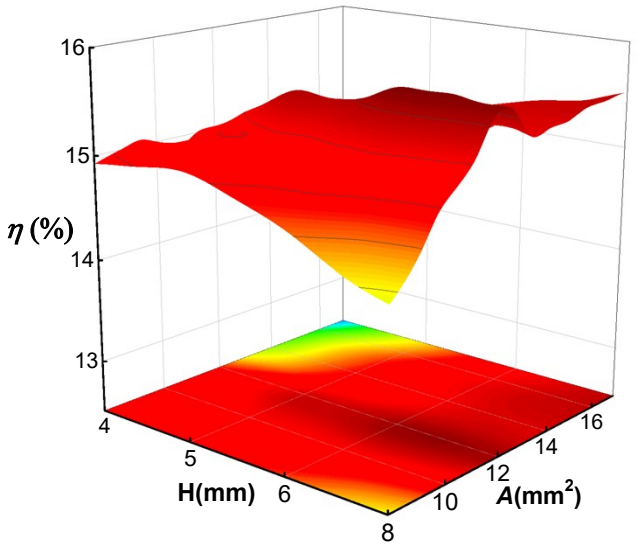

Supplementary Fig. 23. Theoretical conversion efficiency (η) as a function of single-leg hight and cross-sectional area.

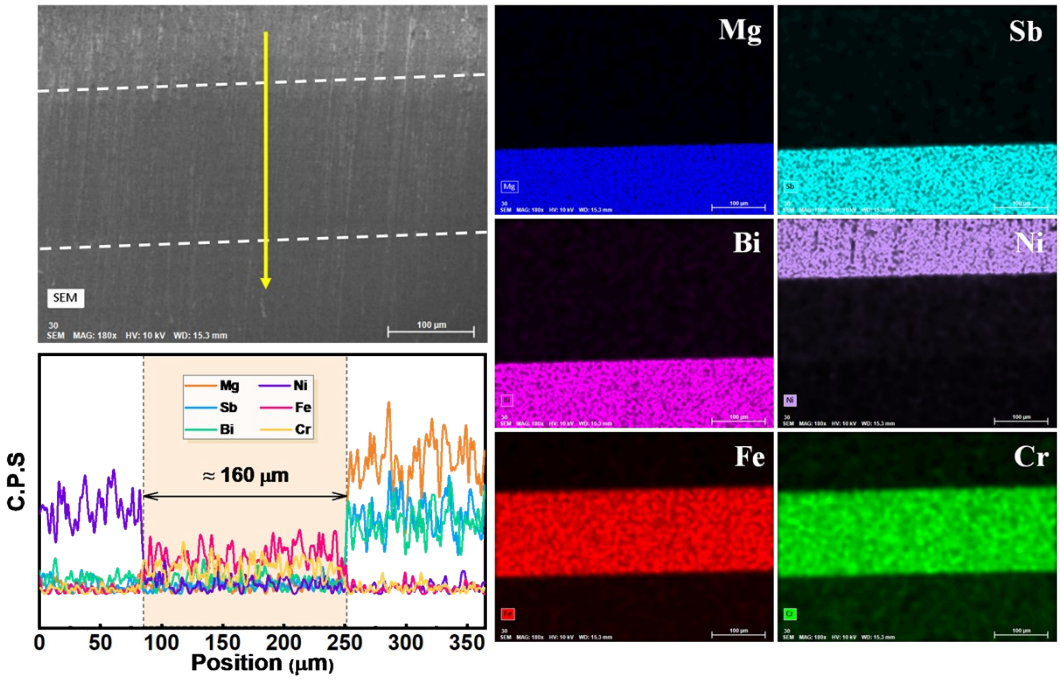

Supplementary Fig. 24. The SEM and its elemental mapping of TE leg near the interface between the material and barrier layer.

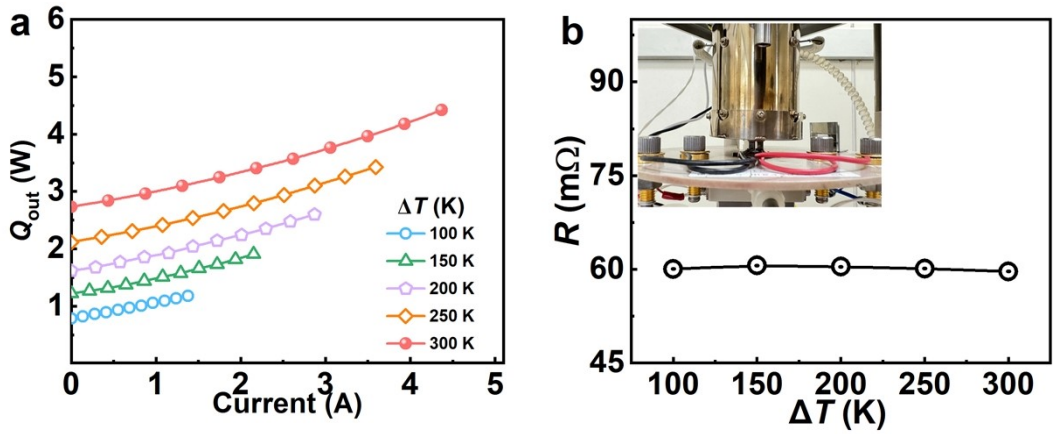

Supplementary Fig. 25. a The data of a TE module by current dependence heat flow, **b** the internal resistance.

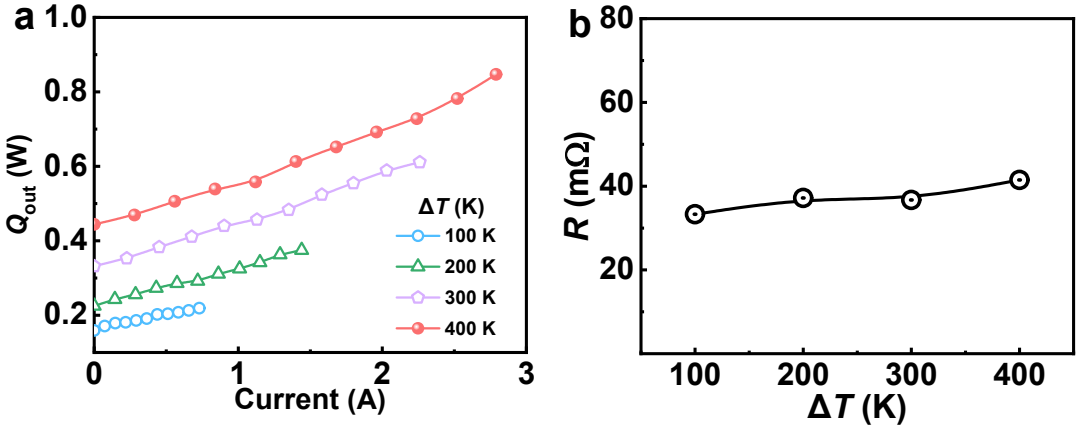

Supplementary Fig. 26. a The data of a single leg by current dependence heat flow, **b** the internal resistance.

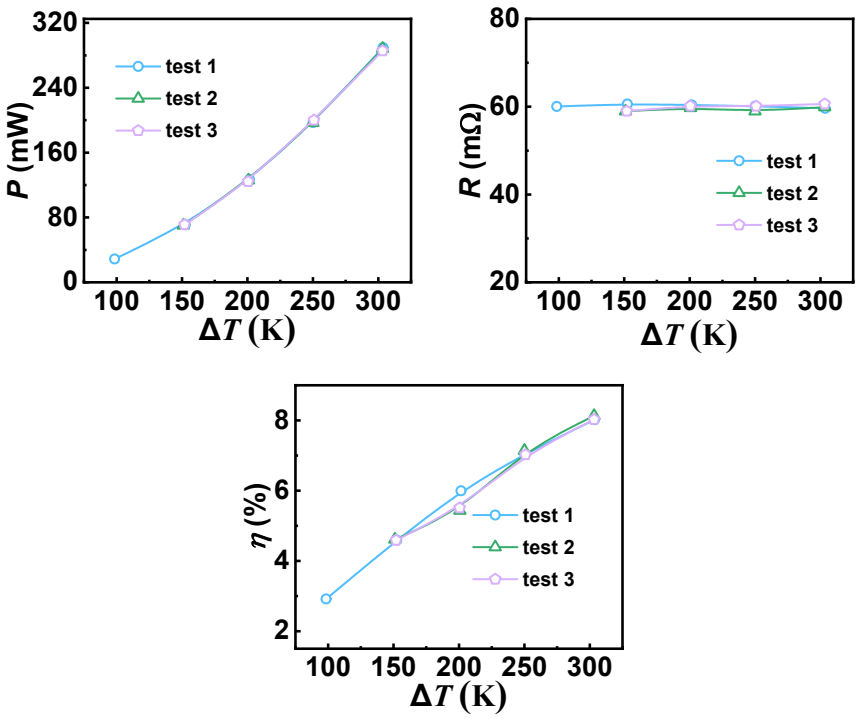

Supplementary Fig. 27. The repeated test of TE module under different temperature differences.

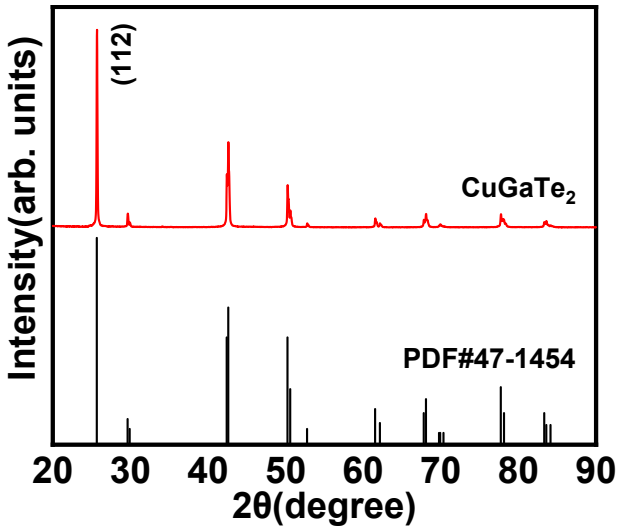

Supplementary Fig. 28. The XRD pattern of synthesized $CuGaTe_2$ sample at room temperature.

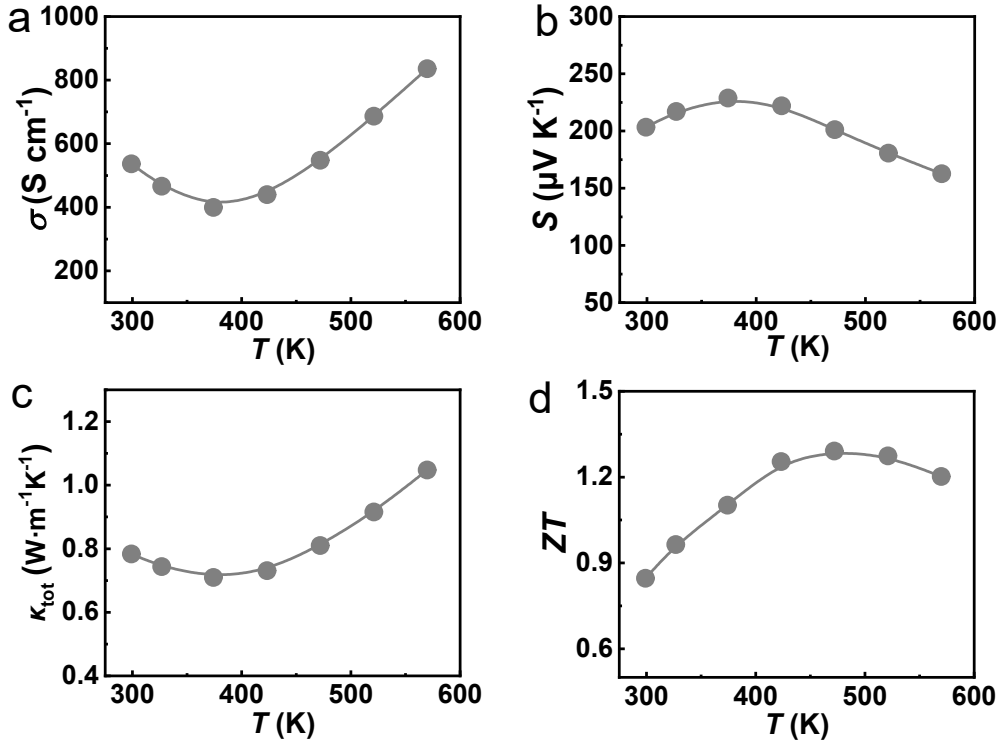

Supplementary Fig. 29. The properties of p-type MgAgSb properties. **a** σ, **b** S, **c** κ_{tot}, **d** ZT value.

Supplementary Table 1. The number of grains counted, mean grain size, median grain size and standard deviation for x=0, x=0.005, x=0.009 samples.

sample	Number of grains counted	Mean (μm)	Median (μm)	Std. dev. (μm)
x=0	463	5.04	4.54	1.54
x=0.005	455	5.6	4.88	1.57
x=0.009	468	5.2	4.59	1.47

Supplementary Table 2. EPMA point analysis results in the x=0.005 sample.

Position	Mg (at.%)	Sb (at.%)	Bi (at.%)	Cu (at.%)	Ga (at.%)	Te (at.%)
1	61.2	24.2	7.2	6.1	1.0	0.29
2	58.0	25.0	7.3	6.0	3.3	0.30
3	55.0	20.6	5.5	13.1	5.6	0.24
4	60.9	22.1	6.2	9.6	1.0	0.28
5	51.5	15.7	4.1	20.1	8.4	0.19

Supplementary Table 3. EPMA point analysis results in the x=0.009 sample.

Position	Mg (at.%)	Sb (at.%)	Bi (at.%)	Cu (at.%)	Ga (at.%)	Te (at.%)
1	66.0	25.3	7.1	0.84	0.42	0.16
2	64.7	26.3	7.3	0.76	0.55	0.17
3	64.2	24.9	8.3	1.86	0.46	0.16
4	69.4	23.6	6.5	0.12	0.09	0.15
5	64.4	26.1	7.8	0.50	0.85	0.16

Supplementary Tables 4. Parameters for the κ_{lat} calculation of Mg_3Sb_2-based materials in Debye-Callaway model.

Parameters	Descriptions	Values
A_N	Fitted parameter of U process	5.7
Γ_M	The mass disorder scattering parameter	0.1094
Γ_S	The strain field disorder parameter	0.2344
d	Average grain size	5.6 μm
N_D	Dislocation density	6.4×10^{15} m^{-2}
B_D	Burger's vector	4.6 Å
γ	Grüneisen parameter	2.11
v_l	Longitudinal sound velocity	3677 m s^{-1}
v_t	Transverse sound velocity	1781 m s^{-1}
N_p	Number density of precipitates	6.6×10^{20} m^{-3}
R	Average radius for the precipitates	25×10^{-9} m
ΔD	Density difference between matrix and precipitates	3600 Kg m^{-3}
K	Bulk modulus of Mg_3Sb_2	35 GPa
v_p	Poisson's ratio	0.35

Lattice strain is evaluated through the Williamson-Hall analysis.

The Williamson-Hall method is employed to estimate the internal strain of the samples.[3]

$$\beta cos\theta = \varepsilon_{XRD} 4sin\theta + \frac{\lambda}{d_{XRD}} \#(S1)$$

where β, θ, λ, ε_{XRD}, d_{XRD} stand for the full-width half maximum (in radians), diffraction angle of peak, wavelength of the radiation (1.54056 Å), internal strain and crystallite domain size, respectively.

Debye-Callaway model

The Debye-Callaway model is applied to analyze the contributions of various phonon scattering mechanisms, as expressed by the following equation:[4]

$$\kappa_{lat} = \frac{k_B}{2\pi^2 v}\left(\frac{k_B T}{\hbar}\right)^3 \int_0^{\frac{\theta_D}{T}} \tau_{tot}(x) \frac{x^4 e^x}{\left(e^x - 1\right)^2} dx \#(S2)$$

Together with the coefficient, the integrand characterizes the spectral lattice thermal conductivity (κ_s), expressed as:

$$\kappa_s = \frac{k_B}{2\pi^2 v}\left(\frac{k_B T}{\hbar}\right)^3 \tau_{tot}(x) \frac{x^4 e^x}{\left(e^x - 1\right)^2} \#(S3)$$

where $x=\hbar\omega/k_B T$, k_B, v, $\hbar$, θ_D, τ_{tot} represent the reduced phonon frequency, Boltzmann constant, mean sound velocity, reduced Plank constant, Debye temperature and phonon relaxation time, respectively. Here, this model manily analyzes the phonon-phonon Umklapp process (U), grain boundary scattering (B), point defect scattering (PD), dislocations scattering (DC), strain scattering (DS) and nanoprecipitates (NP).[5]

$$\tau_{tot}^{-1} = \tau_U^{-1} + \tau_{PD}^{-1} + \tau_B^{-1} + \tau_{DC}^{-1} + \tau_{DS}^{-1} + \tau_{\mathrm{NP}}^{-1} \#(S4)$$

The Umklapp phonon-phonon scattering (U),[6]

$$\tau_U^{-1} = A_N \frac{\hbar \gamma^2 \omega^2 T}{M v_s^2 \theta_D} \exp\left(-\frac{\theta_D}{3T}\right) \#(S5)$$

where A_N, γ, M denote the fitting parameters corresponding to the Umklapp scattering time, Grüneisen parameter and average atomic mass, respectively. The coefficient A_N can be derived from single-crystal data.[7]

The grain boundary scattering (B),[8]

$$\tau_B^{-1} = \frac{v}{d} \#(S6)$$

where d is the average grain size.

The point defect phonon scattering (PD)[9],

$$\tau_{PD}^{-1} = \frac{V\omega^4}{4\pi v^3}(\Gamma_M + \Gamma_S) \#(S7)$$

where V, Γ_M, Γ_S denote the unit atomic volume, mass and strain field fluctuations, respectively. The calculation of mass and strain field fluctuations can be expressed as.[10]

$$\Gamma_M = \frac{\sum_{i=1}^{n} c_i \left(\frac{\overline{M_i}}{\tilde{M}}\right)^2 \Gamma_{M,i}}{\sum_{i=1}^{n} c_i}, \Gamma_{M,i} = \sum_k f_i^k \left(1 - \frac{M_i^k}{\overline{M_i}}\right)^2 \#(S8)$$

$$\tilde{M} = \frac{\sum_{i=1}^{n} c_i \overline{M_i}}{\sum_{i=1}^{n} c_i} \#(S9)$$

where c_i is number of atoms on site i, M_i^k and f_i^k are the mass and fractional occupancy of the k-th atom, $\overline{M_i}$ denotes the average mass at site i, and $\tilde{M}$ is the average mass of the compound.

$$\Gamma_S = \frac{\sum_{i=1}^{n} c_i \left(\frac{\overline{M_i}}{\tilde{M}}\right)^2 \varepsilon_i \Gamma_{R,i}}{\sum_{i=1}^{n} c_i}, \Gamma_{R,i} = \sum_k f_i^k \left(1 - \frac{R_i^k}{\overline{R_i}}\right)^2 \#(S10)$$

$$\varepsilon_i = \frac{2}{9}\left(6.4\gamma\frac{1+\nu_p}{1-\nu_p}\right)^2 \#(S11)$$

Here, R_i^k and f_i^k denote the radius and fractional occupancy of the k-th atom at site *i*, $\overline{R_i}$ is the average radius at site *i*, ε_i is a coefficient determined by the Grüneisen parameter γ and the Poisson ratio ν_p.

The dislocations scattering (DC) and strain scattering (DS)[11],

$$\tau_{DC}^{-1} = N_D\frac{\bar{V}^{\frac{4}{3}}}{\nu^2}\left(\frac{xk_BT}{\hbar}\right)^3 \#(S12)$$

$$\tau_{DS}^{-1} = 0.6\,{}_xB_D^2N_D(\gamma + \Delta\gamma)^2\frac{xk_BT}{\hbar}\left\{\frac{1}{2} + \frac{1}{24}\left(\frac{1-2\upsilon_p}{1-\upsilon_p}\right)^2\left[1 + \sqrt{2}\left(\frac{\nu_l}{\nu_t}\right)^2\right]^2\right\} \#(S13)$$

$$\Delta\gamma = \frac{V_{\mathrm{Mg3Bi2}}C_0K}{k_{\mathrm{B}}T_{\mathrm{a}}}(\gamma\alpha^2 - \alpha\beta) \#(S14)$$

$$\alpha = \frac{V_{\mathrm{Mg3Sb2}} - V_{\mathrm{Mg3Bi2}}}{V_{\mathrm{Mg3Bi2}}} \#(S15)$$

$$\beta = \frac{M_{\mathrm{Mg3Bi2}} - M_{\mathrm{Mg3Sb2}}}{2M_{\mathrm{Mg3Bi2}}} \#(S16)$$

In this expression, N_{D}, B_{D}, C_0, K, T_{a}, γ, ν_p represent the dislocation density, Burgers vector, Mg_3Sb_2 fraction in $Mg_3Sb_{1.5}Bi_{0.5}$, bulk modulus, sintering temperature, Grüneisen parameter and Poisson ratio, respectively.

The nanoprecipitates (NP)[12],

$$\tau_{\mathrm{NP}}^{-1} = v\left[\left(2\pi R^2\right)^{-1} + \left(\frac{4}{9}\pi R^2(\Delta D/D)^2(\omega R/v)^4\right)^{-1}\right]^{-1}N_{\mathrm{P}} \#(S17)$$

where N_{p} represents the number density of precipitates, R represents the average radius for the precipitates, D is the matrix density and ΔD is the density difference between matrix and precipitates.

Debye temperature θ_{D} is calculated by

$$\theta_D = \hbar v(6\pi^2 n)^{1/3}/k_B \#(S18)$$

where n denote the number of atoms per unit volume.

The mean sound velocity v is estimated by the longitudinal sound velocity (v_l) and transverse sound velocity (v_t)[13]

$$v = [\frac{1}{3}(\frac{1}{v_l^3} + \frac{2}{v_t^3})]^{-1/3} \#(S19)$$

The necessary parameters for the Debye-Callaway model are listed in Table S3.

The calculated minimum lattice thermal conductivity

The lower limit of lattice thermal conductivity can be approximated using the diffusive thermal transport model.[14]

$$\kappa_{diff} = 0.76 k_B n^{\frac{2}{3}} \frac{1}{3}(2v_t + v_l) \#(S20)$$

where the n, k_B, v_t, v_l denote the number density of atoms, Boltzmann constant, transverse sound velocity and longitudinal sound velocity, respectively.

Single Parabolic Band (SPB) model

It is assumed that carrier scattering is mainly governed by acoustic phonon scattering (r=-1/2), following the single parabolic band model for semiconductors. The Seebeck coefficient and carrier concentration can then be described as:[15]

$$S = \pm \frac{k_B}{e}\left(\frac{\left(r+\frac{5}{2}\right)F_{r+\frac{3}{2}}(\eta)}{\left(r+\frac{3}{2}\right)F_{r+\frac{1}{2}}(\eta)} - \eta\right) \#(S21)$$

$$n = \frac{4\pi\left(2k_B T m^*\right)^{\frac{3}{2}}}{h^3} F_{\frac{1}{2}}(\eta) \#(S22)$$

$$F_n(\eta) = \int_0^\infty \frac{x^n}{1 + e^{x-\eta}} dx \#(S23)$$

where the η, k_B, m_b* denote reduced chemical potential, Boltzmann constant and band mass of a single Fermi pocket, respectively.

TE module measurement

The conversion efficiencies are measured using a commercial Advanced Riko Mini-PEM apparatus under steady-state conditions. During measurement, the cold-side temperature is fixed at 300 K, while the hot-side temperature was controlled by the built-in heater. The hot-side temperature (T_h), cold-side temperature (T_c), electrical output power (P_{out}) and output heat flow (Q_{out}) record simultaneously, and the conversion efficiency is calculated according to:[16]

$$\eta_{max} = \frac{P_{out}}{P_{out} + Q_{out}} \#(S24)$$

Parasitic heat loss is one of the major sources of uncertainty in TE efficiency measurement, and it mainly includes convection and radiation losses. In this work, the device tests are performed under vacuum throughout the measurement, which is a standard and effective way to suppress convection heat loss. However, radiative heat loss cannot be fully eliminated, especially for finite-size devices. For the single-leg measurements, the device cross-sectional area is smaller than the 10×10 mm^2 base area of the Mini-PEM heat-flow stage. Therefore, for the single-leg measurements, the built-in radiation-calibration function of the commercial Mini-PEM software is applied. By

contrast, for the two-pair module, the device footprint matched the 10×10 mm^2 stage area and thus no additional radiation correction is required. Regarding uncertainty, based on the commercial calorimetric protocol of the Mini-PEM, an uncertainty of approximately ~10% exists in the measured heat flow and efficiency values. In addition, we have clarified that the achieved device efficiencies are a direct consequence of the combined effects of: (i) the high broad-temperature thermoelectric performance of the optimized n-type material, including its high near-room-temperature and mid-temperature *ZT*; (ii) the low contact resistance and chemically stable interfaces, which reduce parasitic interfacial losses; and (iii) the device geometry optimized by finite-element numerical simulation.

Numerical Modelling

Numerical simulations are performed using the commercial COMSOL Multiphysics software, incorporating the Seebeck, Thomson, and Peltier effects as well as Joule heating.[17, 18]

$$\nabla(\kappa\nabla T) + \frac{J^2}{\sigma} - TJ.\left[\left(\frac{\partial S}{\partial T}\right)\nabla T + (\nabla S)_T\right] = 0\#(S25)$$

$$\nabla \cdot J = 0\#(S26)$$

$$J = -\sigma(\nabla V + S\nabla T)\#(S27)$$

where T represents the Kelvin temperature, κ denotes the thermal conductivity, σ is the electrical conductivity, S stands for the Seebeck coefficient, J denotes the current density and V is the electrostatic potential, respectively.

Weighted mobility calculation

$$\mu_w = 331\sigma\left(\frac{T}{300}\right)^{-\frac{3}{2}}\left[\frac{\exp\left[\frac{|S|}{\frac{k_B}{e}} - 2\right]}{1+\exp\left[-5\left(\frac{|S|}{\frac{k_B}{e}} - 1\right)\right]} + \frac{\frac{3\,|S|}{\pi^2\frac{k_B}{e}}}{1+\exp\left[5\left(\frac{|S|}{\frac{k_B}{e}} - 1\right)\right]}\right] \#(S28)$$

where T, k_B, e denote the Kelvin temperature, Boltzmann constant and electron charge.

Supplemental references

1 (Eds: P. Villars, H. Okamoto), Springer-Verlag Berlin Heidelberg & Material Phases Data System (MPDS), Switzerland & National Institute for Materials Science (NIMS), Japan.

2 (Eds: P. Villars, H. Okamoto), Springer-Verlag Berlin Heidelberg & Material Phases Data System (MPDS), Switzerland & National Institute for Materials Science (NIMS), Japan.

3 M. Ghasemi Hajiabadi, M. Zamanian and D. Souri, *Ceram. Int.*, 2019, **45**, 14084-14089.

4 J. Callaway, *Phys. Rev.*, 1959, **113**, 1046-1051.

5 F. C. Schwerer, J. W. Conroy and S. Arajs, *J. Phys. Chem. Solids*, 1969, **30**, 1513-1525.

6 G. A. Slack and S. Galginaitis, *Phys. Rev.*, 1964, **133**, A253-A268.

7 Y. Pan, M. Yao, X. Hong, Y. Zhu, F. Fan, K. Imasato, Y. He, C. Hess, J. Fink, J. Yang, B. Büchner, C. Fu, G. J. Snyder and C. Felser, *Energy Environ. Sci.*, 2020, **13**, 1717-1724.

8 Z. Wang, J. E. Alaniz, W. Jang, J. E. Garay and C. Dames, *Nano Lett.*, 2011, **11**, 2206-2213.

9 P. G. Klemens, *Phys. Rev.*, 1960, **119**, 507-509.

10 J. Yang, G. P. Meisner and L. Chen, *Appl. Phys. Lett.*, 2004, **85**, 1140-1142.

11 S. I. Kim, K. H. Lee, H. A. Mun, H. S. Kim, S. W. Hwang, J. W. Roh, D. J. Yang, W. H. Shin, X. S. Li, Y. H. Lee, G. J. Snyder and S. W. Kim, *Science*, 2015, **348**, 109-114.

12 S. Chen, J. Wei, Z. Kang, X. Miao, D. An, W. Fan and C. Dun, *Chem. Eng. J.*, 2024, **490**, 151404.

13 C. L. Wan, W. Pan, Q. Xu, Y. X. Qin, J. D. Wang, Z. X. Qu and M. H. Fang, *Phys. Rev. B*, 2006, **74**, 144109.

14 M. T. Agne, R. Hanus and G. J. Snyder, *Energy Environ. Sci.*, 2018, **11**, 609-616.

15 J. Mao, H. S. Kim, J. Shuai, Z. Liu, R. He, U. Saparamadu, F. Tian, W. Liu and Z. Ren, *Acta Mater.*, 2016, **103**, 633-642.

16 S. Bano, R. Chetty, J. Babu and T. Mori, *Device*, 2024, **2**, 100408.

17 A. Nozariasbmarz, R. A. Kishore, B. Poudel, U. Saparamadu, W. Li, R. Cruz and S. Priya, *ACS Appl. Mater. Interfaces*, 2019, **11**, 40107-40113.

18 Q. Zhang, J. Liao, Y. Tang, M. Gu, C. Ming, P. Qiu, S. Bai, X. Shi, C. Uher and L. Chen, *Energy Environ. Sci.*, 2017, **10**, 956-963.